



Interaction of CO with hydrous ruthenium oxide and development of a chemoresistive ambient CO sensor

Adedunni Adeyemo^a, Gary Hunter^b, Prabir K. Dutta^{a,*}

^a Department of Chemistry, The Ohio State University, 100 West 18th Avenue, Columbus, OH 43210-1185, United States

^b NASA Glenn Research Center, Cleveland, OH 44135, United States

ARTICLE INFO

Article history:

Received 15 August 2010

Received in revised form 7 December 2010

Accepted 15 December 2010

Available online 22 December 2010

Keywords:

Infrared spectroscopy

Room temperature gas sensor

CO oxidation

X-ray photoelectron spectroscopy

Metal oxide sensor

Hydrated ruthenium oxide

ABSTRACT

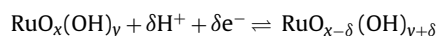
Hydrated ruthenium oxide ($\text{RuO}_x(\text{OH})_y$), the material of interest in this study was prepared by reaction of an aqueous solution of ruthenium chloride with base. This material was amorphous, made up of 20–50 nm particles and contains Ru(III) and Ru(IV), as determined by X-ray photoelectron spectroscopy. The conductivity of thick films of $\text{RuO}_x(\text{OH})_y$ decreased in the presence of CO in a background of air and this change was reversible. Infrared spectroscopy showed the formation of carbonates in the presence of CO, which disappeared upon replacement of CO with O₂. Upon heating $\text{RuO}_x(\text{OH})_y$, there was a gradual conversion to crystalline RuO₂ beyond 200 °C. With these heated materials, the resistance change in the presence of CO at room temperature also gradually diminished. We propose that oxidation of CO on $\text{RuO}_x(\text{OH})_y$ leads to reduction of the ruthenium and a decrease in conductivity. With the conversion to crystalline RuO₂ upon heating, the material becomes metallic and conductivity changes are diminished. The change in conductivity of $\text{RuO}_x(\text{OH})_y$ with CO provides a convenient platform for an ambient CO sensor. Such a device also does not show interference from hydrocarbons (2000 ppm), ammonia (150 ppm), CO₂ (2000 ppm), NO (15 ppm) and NO₂ (15 ppm).

© 2010 Elsevier B.V. All rights reserved.

1. Introduction

Ruthenium oxide (RuO₂) is an important technological material. In particular, its electrical properties are dependent on its structure, with the room temperature conductivity of single crystalline RuO₂ reported as high as ~10⁴ S cm⁻¹ [1], poly crystalline RuO₂ ~10³ S cm⁻¹ [2] and amorphous hydrous RuO₂ is ~1 S cm⁻¹ [3]. In its crystalline form, RuO₂ adopts a rutile structure, and exhibits metallic-like conductivity. The crystalline form of RuO₂ is used in the electronics industry as electrodes in integrated circuits [4], and as electrodes for production of hydrogen, chlorine and oxygen [5,6]. The catalysis applications of RuO₂ include water splitting [7,8], oxidation of methanol and ethanol [9] and carbon monoxide oxidation [10].

The hydrated form of ruthenium oxide, $\text{RuO}_x(\text{OH})_y$ is an amorphous material and finds use in the power industry as supercapacitors [11,12]. The supercapacitor performance of $\text{RuO}_x(\text{OH})_y$ stems from its ability to reversibly incorporate protons and electrons, as shown below [11,12]:



Several studies have discussed the structure of $\text{RuO}_x(\text{OH})_y$ [11–13]. The picture that emerges is that the nanoparticles present in $\text{RuO}_x(\text{OH})_y$ consist of disordered arrangements of RuO₆ chains, capped off by OH groups. Within the grains, conductivity is considered to be primarily metallic-like arising from the d-band structure. Conduction involves electron hopping between the particles, and this process is dependent on the size of the particle. Optimization of the supercapacitor performance of $\text{RuO}_x(\text{OH})_y$ has focused on studies of the interfacial electron transfer between the nanoparticles, and control of the microstructure [13]. For example, a hydrated form of mesoporous RuO₂ was reported to have excellent capacitive behavior [14]. Hydrous amorphous ruthenium oxide is also a carbon monoxide oxidation catalyst under ambient conditions, however, the catalytic activity is strongly dependent on the thermal history of the samples, and diminishes as the material is heated [15].

In this paper, we focus on the electronic conductivity of hydrated amorphous ruthenium oxide and changes thereof in the presence of carbon monoxide. Using information from infrared spectroscopy, we propose a mechanism for the observed changes in electrical properties. The change in conductivity with CO at room temperature was also exploited to develop an ambient CO monitor. There is need for low power, solid state, miniaturizable CO sensors, and to the best of our knowledge, this study reports the first example of use of hydrated amorphous ruthenium oxide as an ambient

* Corresponding author.

E-mail addresses: dutta.1@osu.edu, dutta@chemistry.ohio-state.edu (P.K. Dutta).

chemoresistive CO sensor. Most semiconducting metal oxides such as TiO_2 [16,17], polyaniline– TiO_2 [18], $\text{Au}-\text{Co}_3\text{O}_4$ [19], SnO_2 [20], detect CO at high temperatures. Modifications of some metal oxides by addition of noble metals as in $\text{Pt}-\text{SnO}_2$ [21] and $\text{Au}-\text{ZnO}$ [22] can lower the temperature of operation. Metallic RuO_2 is used as a gate material in field effect sensor devices [23].

2. Experimental

2.1. Materials synthesis

Hydrated ruthenium oxide ($\text{RuO}_x(\text{OH})_y$) was prepared by a precipitation method [24]. To a stirred 0.1 M aqueous solution of ruthenium chloride ($\text{RuCl}_3 \cdot x\text{H}_2\text{O}$ Sigma–Aldrich), 0.3 M sodium hydroxide (Mallinckrodt 98.7%) solution was added drop-wise until pH 7. The resulting precipitate was washed several times until chloride free (tested with AgNO_3), and dried in air at room temperature. Heat treatment of $\text{RuO}_x(\text{OH})_y$ was carried out at 100 °C, 200 °C, 300 °C, 400 °C, 500 °C and 600 °C for 10 h each. The resulting powders were crushed in an agate mortar and pestle for 5 min and used for all further experiments.

2.2. Materials characterization

Thermogravimetric analysis (TGA) experiments were carried out with PerkinElmer TGA 7, with a Thermal Analysis Controller, TAC 7/DX. A ramp rate of 10 °C/min in nitrogen gas flow of 40 cc/min was used. A Rigaku Geigerflex X-ray diffractometer with Ni-filtered $\text{Cu K}\alpha$ radiation was used for powder diffraction measurements. A Tecnai F20 with field emission 200 kV STEM and X-TWIN lens was used to elucidate the microstructure and particle size. The Kratos AXIS Ultra X-ray photoelectron spectrometer (XPS) with an Al source was used for all XPS analysis. A 13 kV voltage with a 10 mA current and pass energy of 20 eV at 0.1 eV resolution was used. CasaXPS Version 2.3.15 software was used for the deconvolution of the XPS data. A Shirley background was used for all data processing. The binding energies were calibrated relative to the Na 1s peak at 1072 eV.

Diffuse reflectance infrared Fourier transform spectroscopy (DRIFTS) analysis was carried out in a controlled environment cell (Pike Technologies) with a ZnSe window in a PerkinElmer Spec400 spectrometer. Samples of 25 wt% of $\text{RuO}_x(\text{OH})_y$ dispersed in spectral grade KBr (Pike Technologies) was used for each experiment. Certified mixtures of CO, 2000 ppm in N_2 (Praxair), 100% CO_2 (Praxair) and 21% oxygen in argon (Praxair) were used with gas flow rates of 60 cc/min. Scans were collected in the range 4000–850 cm^{-1} with a resolution of 4 cm^{-1} . All spectral subtractions were done with the Spectrum 6.3.1 software (PerkinElmer). The subtraction factor was varied between 0.932 and 1.000 until the ν_{CH} stretching vibrations peaks at 2800–2950 cm^{-1} were minimized. A mercury cadmium telluride (MCT) detector was used for the IR measurements.

2.3. Resistance measurements

Alumina substrates (15 mm × 10 mm) with interdigitated gold lines of 0.25 mm spacing were obtained from Case Western Reserve University Electronics Design Center. Gold lead wires (Alfa Aesar, 99.99%) were connected with gold paste (Heraeus). The electrodes were heat treated at 600 °C for 3 h in order to remove organic binders from the gold paste. The $\text{RuO}_x(\text{OH})_y$ particles were suspended in water (5% by weight) by sonication for 1 h. The suspension was drop coated onto the electrodes and allowed to dry in air for 4–6 h.

All tests were done with a quartz tube housed in a temperature programmable furnace (Lindberg Blue, TF55035A). Measurement

protocol consisted of flowing various volumes of certified mixtures of carbon monoxide 2000 ppm in N_2 (Praxair), 50% oxygen in N_2 (Praxair) and nitrogen (Praxair) over the devices to give 250–1000 ppm CO in 21% oxygen, balanced with nitrogen in order to keep the flow rate constant. Certified premixed carbon dioxide 2000 ppm in nitrogen (Praxair), methane 2000 ppm in nitrogen (Praxair), propane 2000 ppm in nitrogen (Praxair), and ammonia 300 ppm in nitrogen (Praxair) were used. Gas concentrations were varied by varying the flow of each gas with Sierra mass flow controllers controlled by a National instruments card (NI-6703) and operated by a Labview program. Resistance measurements were made with a HP34970A at a scan rate of 0.1 Hz. Tests were carried out at 25 °C with a gas flow rate of 100 cc/min for all experiments.

3. Results

3.1. Synthesis and characterization of $\text{RuO}_x(\text{OH})_y$

As expected from earlier reports [24], a brown aqueous solution of $\text{RuCl}_3 \cdot x\text{H}_2\text{O}$ changes to a black solution as the pH was gradually increased. When stirring was stopped at pH 7, a black solid collected at the bottom leaving a clear liquid at the top. The precipitate ($\text{RuO}_x(\text{OH})_y$) was separated by centrifugation and forms the subject matter of this paper.

The weight loss upon heating of $\text{RuO}_x(\text{OH})_y$ was determined by thermogravimetric analysis, and the data is shown in Fig. 1a. The weight loss occurs in three stages, a moderately rapid loss until ~225 °C, a gradual loss until 1125 °C, followed again by a rapid loss. These stages have been described in literature as arising from water loss via loss of H_2O and OH groups and finally the reduction to metal beyond 1050 °C [25]. Based on the TGA data shown in Fig. 1a, we estimate a ~22% drop in mass for $\text{RuO}_x(\text{OH})_y$ due to water/OH loss over the temperature range of 25–325 °C, indicating a molecular formula of $\text{RuO}_2 \cdot 2\text{H}_2\text{O}$. Fig. 1b shows the diffraction pattern of the as-synthesized $\text{RuO}_x(\text{OH})_y$, the absence of peaks indicating that it is an amorphous material. Fig. 1c shows a TEM image for the $\text{RuO}_x(\text{OH})_y$. The particle size based on the analysis of ~100 particles is found to be between 20 and 50 nm.

X-ray photoelectron spectroscopy of $\text{RuO}_x(\text{OH})_y$ in the O 1s and Ru 3d region is shown in Fig. 2. Curve deconvolution of the oxygen 1s region (Fig. 2a), results in three peaks at 528.0, 529.0 and 531.0 eV, indicating the presence of multiple oxygen species. Based on the literature [26], these peaks are assigned in order of increasing binding energy to Ru–O–Ru, Ru–OH and Ru– H_2O , respectively. However, our infrared studies discussed later show the presence of carbonates on the as-synthesized material, and carbonate oxygen can also contribute to the 531 eV peak [27].

The Ru 3d region for $\text{RuO}_x(\text{OH})_y$ exhibits two broad bands at ~280 and ~285 eV (Fig. 2b), the intensity arising from the $3d_{5/2}$ and $3d_{3/2}$ electrons. Several studies have reported the XPS of different forms of hydrated ruthenium oxide [25,26,28–30]. There is general consensus that the signal appears from a mixture of Ru (III) and Ru(IV), which causes the broad bands. In addition, the hydroxyl and oxygen functionalities surrounding the Ru also lead to broadening, and therefore makes the deconvolution of the Ru 3d region complicated. There is also contribution from the C 1s in this binding energy range. The best fit was obtained with six peaks at 279.3, 280.1, 282.1, 283.6, 284.5 and 295.7 eV. The peaks at 279.3 and 283.6 eV are assigned to hydrous Ru(III) and 280.1 and 284.5 eV to Ru(IV). Since the starting material is $\text{RuCl}_3 \cdot x\text{H}_2\text{O}$, we discount the formation of Ru(0) in the $\text{RuO}_x(\text{OH})_y$ since treatment with base should not result in reduction. The other two peaks at 282.1 and 285.7 eV are assigned to C 1s from carbonaceous impurities and carbonate respectively [25–27], the presence of carbonate is confirmed by infrared spectroscopy.

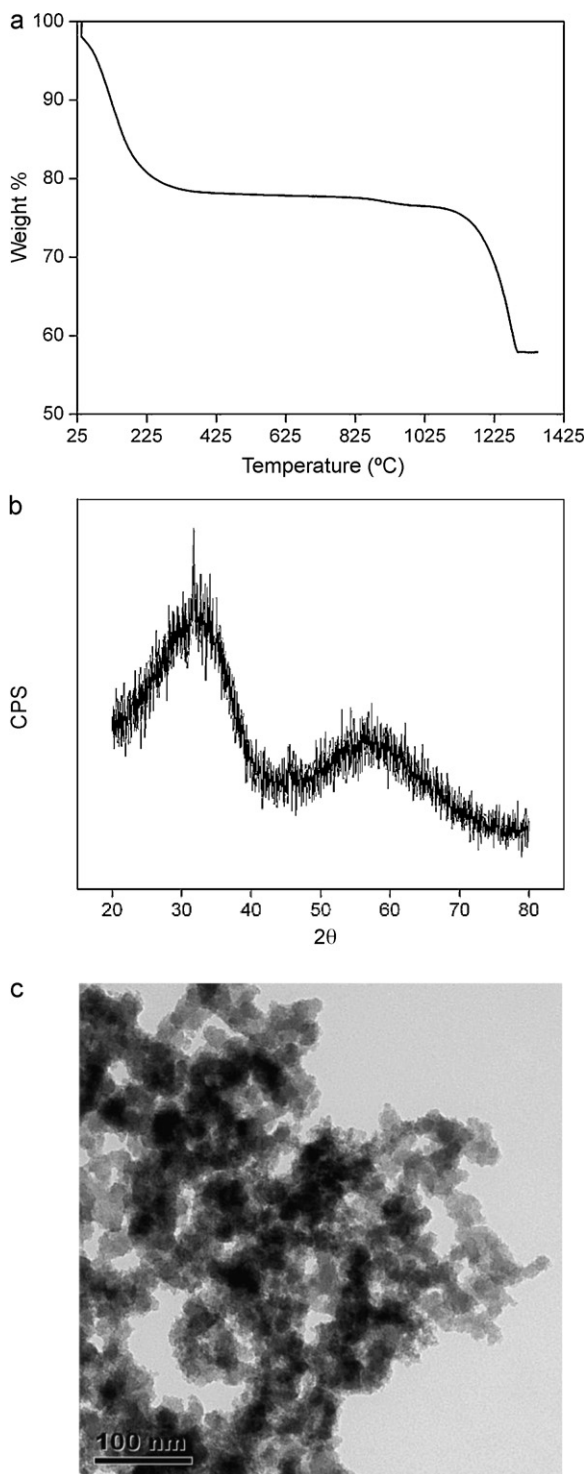


Fig. 1. (a) Thermogravimetric analysis of $\text{RuO}_x(\text{OH})_y$ (ramp rate of $10^\circ\text{C}/\text{min}$ in a nitrogen gas flow of $40 \text{ cc}/\text{min}$), (b) XRD pattern of $\text{RuO}_x(\text{OH})_y$, and (c) TEM image of $\text{RuO}_x(\text{OH})_y$.

3.2. Interaction of $\text{RuO}_x(\text{OH})_y$ with CO

3.2.1. Resistance changes

Fig. 3 shows the changes in resistance of a thick film of $\text{RuO}_x(\text{OH})_y$ upon repeated exposure to 250 ppm CO at 25°C in a background of dry 21% O_2 (the rest is N_2). There is a decrease in baseline resistance upon initiation of the measurement, and is attributed to drying of the sample. The baseline does stabilize with

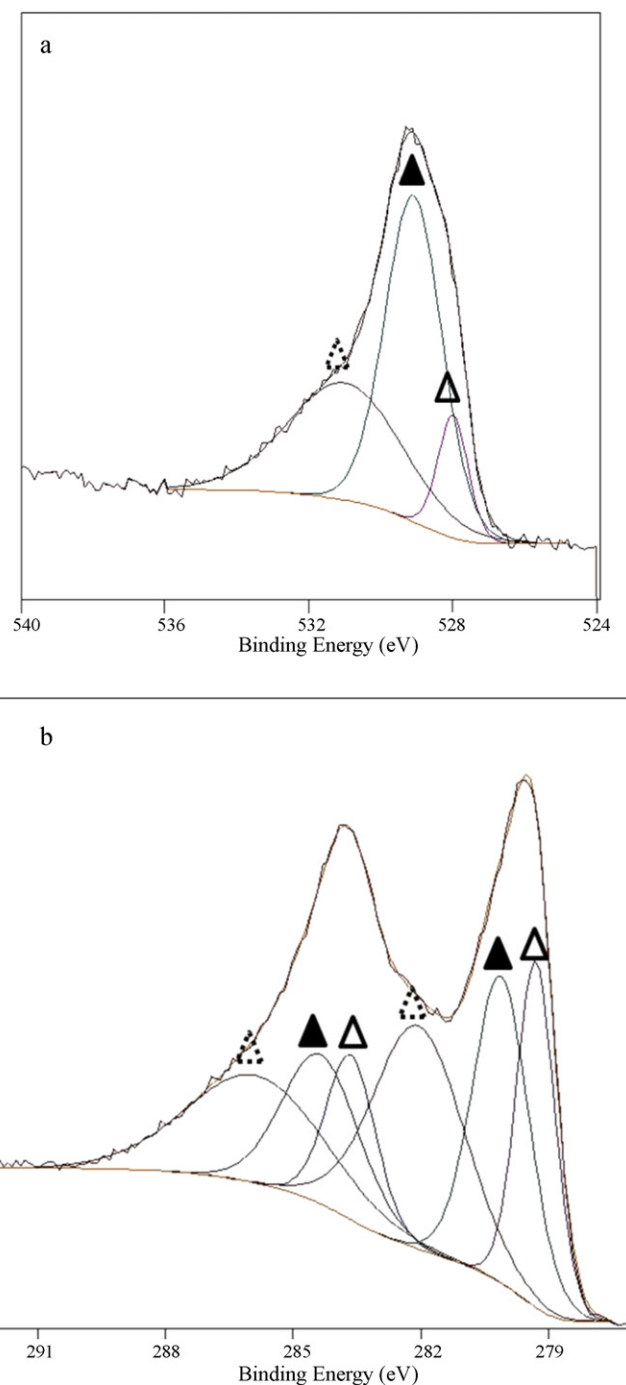


Fig. 2. XPS spectra of $\text{RuO}_x(\text{OH})_y$, (a) O 1s region: \triangle $\text{Ru}-\text{O}-\text{Ru}$, \blacktriangle $\text{Ru}-\text{OH}$ and \diamond $\text{Ru}-\text{H}_2\text{O}/\text{Ru}-\text{carbonate}$ and (b) Ru 3d region: \triangle $\text{Ru}(\text{III})$, \blacktriangle $\text{Ru}(\text{IV})$ and \diamond carbon 1s carbonaceous impurities (282.1) and carbonates (285.7 eV).

time. There is an increase in resistance with CO, and a decrease as the CO is turned off in the gas stream over the film. This cycle can be repeated numerous times (~ 100).

3.2.2. In situ infrared spectroscopy

Diffuse Reflectance Infrared Fourier Transform Spectroscopy (DRIFTS) was used to monitor the surface of $\text{RuO}_x(\text{OH})_y$ as O_2 and CO was passed over the surface. Fig. 4a shows the infrared spectrum of the as-synthesized sample, Fig. 4b after passing O_2 (21%) over the sample for 150 min, Fig. 4c after 2000 ppm CO flowed over the sample shown in Fig. 4b for 15 min, 21% Oxygen was flowed over the sample shown in Fig. 4c for 30 min then the cell was closed off

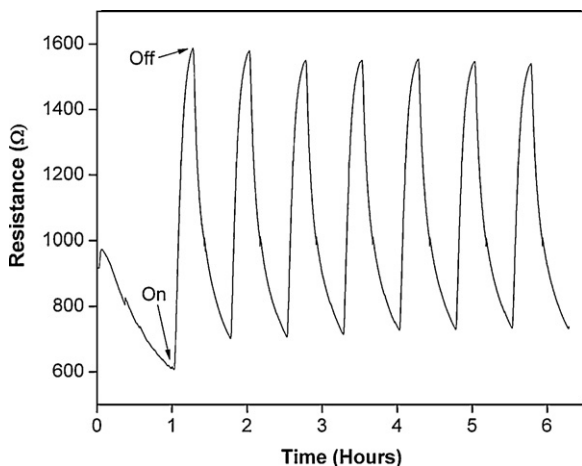


Fig. 3. Changes in resistance of $\text{RuO}_x(\text{OH})_y$ with repeated exposure of to 250 ppm CO in 21% Oxygen at 25 °C.

for 45 min after which Fig. 4d was recorded, Fig. 4e after O₂ (21%) exposure for 150 min over the sample shown in Fig. 4c and f is after CO₂ exposure of the sample shown in Fig. 4b. In these spectra, there are changes observed over several regions. Fig. 4a shows that the as-synthesized sample shows bands in the carbonate and water regions, which change in flowing air. The best way to visualize these changes was by taking difference spectra, which are shown in Fig. 5. The extent of the subtraction was controlled so the intensity in the C-H stretching region was minimized. The sample treated with air (Fig. 4b) is considered the primary control sample and is used in all the spectral subtractions.

Fig. 5b shows that after exposure to 2000 ppm CO (Fig. 4c and b), new bands at 866, 1038, 1167, 1281, 1311, 1433, 1539, 1617 and 1650 cm⁻¹ are observed in the carbonate region. Bands at 1433,

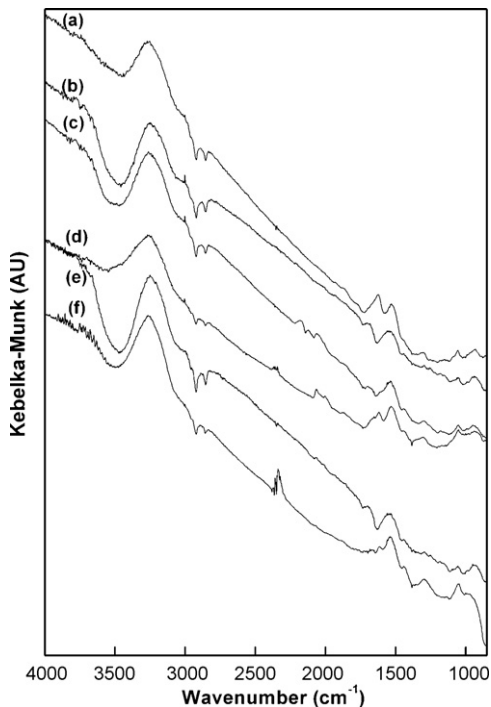


Fig. 4. Diffuse reflectance infrared spectra of $\text{RuO}_x(\text{OH})_y$, (a) initial spectrum, (b) spectrum after exposure to O_2 (21%) for 150 min, (c) spectrum of sample in (b) after CO (2000 ppm in air) exposure for 15 min, (d) spectrum of sample (b) closed off for 45 min after O_2 for 30 mins, (e) spectrum of sample (c) after exposure to O_2 (21%) for 150 min, and (f) spectrum of sample (b) after exposure to CO_2 (25 °C).

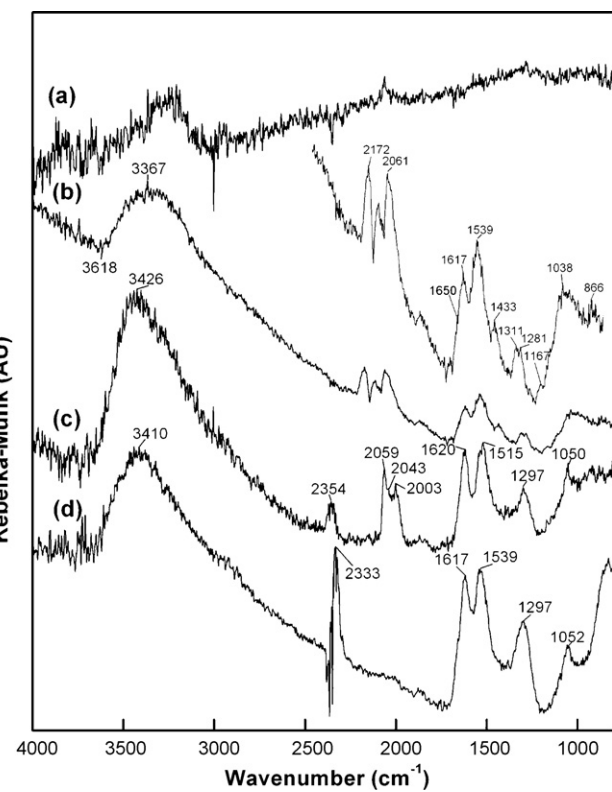


Fig. 5. Difference spectrum of (a) two O₂ (21%) exposures each for 150 min (prior and after CO exposure), (b) O₂ (21%) exposed sample for 150 min and CO (2000 ppm in air) exposure (enhanced y-axis scale in the 1000–2500 cm⁻¹ region), (c) O₂ (21%) exposed sample for 150 min and O₂ (21%) exposed sample for 30 min after CO (2000 ppm in air) exposure and (d) O₂ (21%) exposed sample for 150 min and CO₂ exposure.

1311 and 1167 cm⁻¹ are assigned to monodentate carbonate, bands at 1539, 1281 cm⁻¹ to bidentate carbonates and 1617, 1038 cm⁻¹ to bicarbonates [31–34]. In addition, gas phase CO peaks are observed around 2150 cm⁻¹. In the O-H stretching region, there is increase in intensity at 3367 cm⁻¹ and loss of intensity at 3618 cm⁻¹, there is also an appearance of a shoulder ~1650 cm⁻¹ due to the bending mode of water. Fig. 5c is the difference spectrum for a CO-exposed sample that was treated with flowing oxygen for 30 min, and then the cell was closed off (Fig. 4d and b), and bands at 1050, 1297, 1515 and 1620 cm⁻¹ are observed in the carbonate/bicarbonate stretching region, and there is a loss of the monodentate carbonate peaks, and the water bending mode. In addition, chemisorbed CO bands are observed at 2003, 2043 and 2059 cm⁻¹ and adsorbed CO₂ at 2354 cm⁻¹, in addition to the water band at 3426 cm⁻¹. The difference spectrum between the two long-term exposed O₂ samples is shown in Fig. 5a (Fig. 4e and b), indicating that passing air over a CO-exposed sample over a longer period of time essentially removes all of the new species formed upon CO reaction. The entire cycle of O₂ and CO introduction could be repeated several times, with comparable infrared data. Fig. 5d is the difference spectrum upon CO₂ exposure to RuO_x(OH)_y (Fig. 4f and b). Bands at 1052, 1297, 1539, 1617 cm⁻¹ are observed in the carbonate/bicarbonate region, CO₂ at 2333 cm⁻¹ and the water band at 3410 cm⁻¹.

3.3. Change in properties of $\text{RuO}_x(\text{OH})_y$ with heat treatment

Samples of $\text{RuO}_x(\text{OH})_y$ were heated up to 600°C , and structural as well as resistivity changes were measured under ambient conditions. Fig. 6 shows the powder diffraction pattern of the samples obtained at the various temperatures. Peaks begin to form in

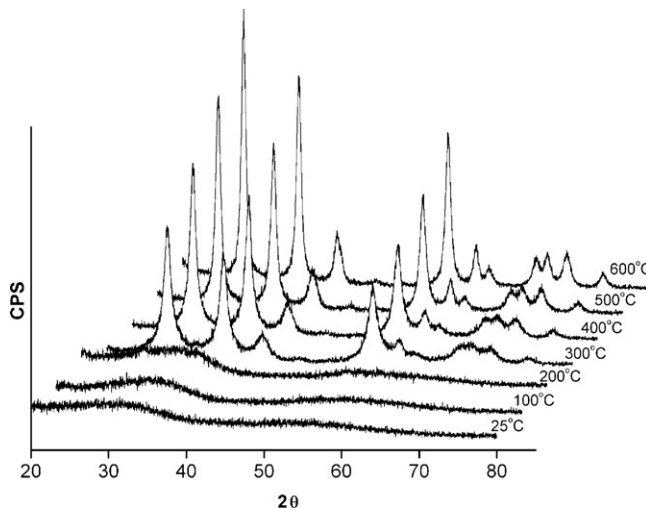


Fig. 6. XRD pattern of samples obtained by heating $\text{RuO}_x(\text{OH})_y$ to different temperatures (data recorded at 25 °C).

the sample heated to 300 °C, and these peaks increase in intensity and sharpen as the heat treatment temperature is increased. The dominant peaks at 28°, 35° and 54° (2θ) correspond to the 110, 101 and 211 reflections of the rutile RuO_2 structure [25]. Correlating this observation with the TGA data in Fig. 1a, it is clear that following the loss of water, the amorphous material is becoming crystalline.

The XPS data were obtained for all the heated samples and the data in the O 1s and Ru 3d region for the sample heated to 600 °C is shown in Fig. 7. As was observed in Fig. 2a, the spectrum of $\text{RuO}_x(\text{OH})_y$ has multiple oxygen species Ru-OH (529.0 eV) and $\text{Ru-H}_2\text{O}$ (531.0 eV) and Ru-O-Ru (528.0 eV) [25]. The ratios of these peaks change with heat treatment, with increasing contributions from Ru-O-Ru (Fig. 7a). In the Ru 3d region, there is a sharpening of the Ru 3d_{5/2} peak with heating and a shift to lower binding energies. This is a reflection of the oxidation of Ru(III) to Ru(IV) as well as the loss of hydroxides on the ruthenium [26]. For the 600 °C treated sample, the Ru 3d XPS data was fit to four peaks (Fig. 7b). The low-binding energy doublet (281.2, 285.4 eV) is assigned to a screened final state and the high-binding energy doublets (282.8, 286.0 eV) to the unscreened final state, both for Ru(IV) typical of crystalline RuO_2 [30].

Fig. 8a shows the change in resistance of the various heat treated samples upon exposure to 500, 250 and 1000 ppm of CO. The relative changes in resistance (R/R_0 , where R is the resistance in the presence of the CO and R_0 is the resistance in the background gas) are shown in Fig. 8b. Clearly, the resistance change diminishes with heat treatment, and is not observable beyond 400 °C.

3.4. CO sensing potential of $\text{RuO}_x(\text{OH})_y$ under ambient conditions

The change in resistance of $\text{RuO}_x(\text{OH})_y$ with CO provides an opportunity for developing a solid state electrochemical ambient CO sensor. Multiple devices were made with $\text{RuO}_x(\text{OH})_y$ and tested in parallel at 25 °C. Fig. 9 shows the response of three devices to 1000, 500, 250, 1000 ppm CO in an air background. Response times and recovery times for the 1000 ppm CO were calculated to be 6 and 11 min (time taken to reach 90% of the steady state signal). The insert in Fig. 9 shows the response with 32 ppm CO over a 12-h period, and the response appears to be stable. We did notice that beyond 16 h, a gradual decrease in signal is observed. Fig. 10 depicts the normalized resistance (R/R_0) to 2000 ppm CO_2 , 1000 ppm methane and propane, 150 ppm ammonia, 15 ppm NO and NO_2 , indicating that the device is selective towards CO.

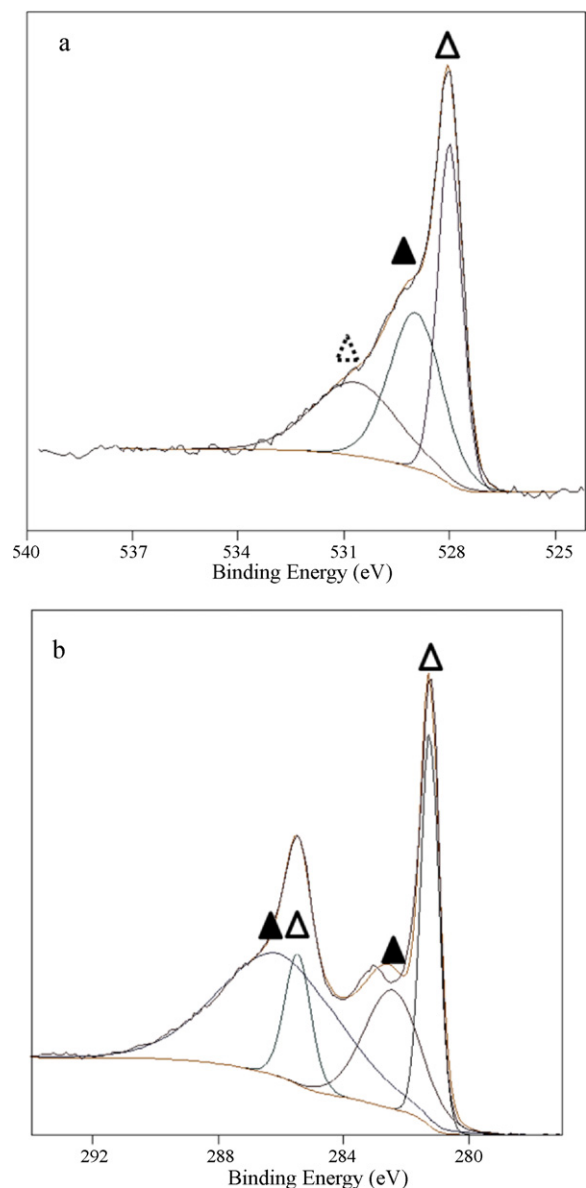


Fig. 7. (a) O 1s XPS spectra of $\text{RuO}_x(\text{OH})_y$ heated to 600 °C: △ Ru-O-Ru, ▲ Ru-OH and ▲ Ru-H₂O and (b) Ru 3d XPS spectra of $\text{RuO}_x(\text{OH})_y$ heated to 600 °C: △ Ru screened final state, ▲ Ru unscreened final state for Ru(IV).

4. Discussion

The primary focus of this discussion is to examine the reactivity of CO on $\text{RuO}_x(\text{OH})_y$ and correlation of the reactivity patterns with the resistance changes of $\text{RuO}_x(\text{OH})_y$ upon exposure to CO. The catalytic activity of $\text{RuO}_x(\text{OH})_y$ towards CO oxidation under ambient conditions has been examined as a function of heat treatment of $\text{RuO}_x(\text{OH})_y$ [15]. It is reported that the untreated as-synthesized samples have negligible catalytic activity, the activity increases upon heating the sample, with the optimum temperature being 150–250 °C (CO conversion of 42.46%), and decreases significantly for samples heated at 450–600 °C [15]. Thus, both as-synthesized $\text{RuO}_x(\text{OH})_y$ and crystalline RuO_2 obtained from heating the $\text{RuO}_x(\text{OH})_y$ beyond 500 °C are poor ambient condition CO oxidation catalysts, yet the change in electrical properties upon exposure to CO is very different (Fig. 8). As-synthesized $\text{RuO}_x(\text{OH})_y$ exhibits marked changes in resistance with CO and $\text{RuO}_x(\text{OH})_y$ heated beyond 500 °C (converted to crystalline RuO_2) exhibiting no change at all.

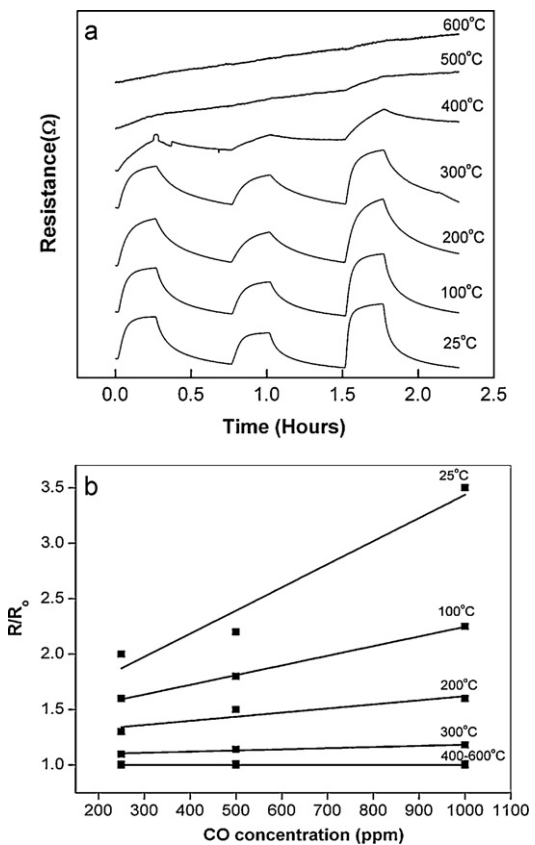


Fig. 8. (a) Change in resistance of samples obtained by heating $\text{RuO}_x(\text{OH})_y$ (25–600 °C) upon exposure to 500, 250 and 1000 ppm CO at 25 °C. (b) Normalized resistance change of samples obtained by heating $\text{RuO}_x(\text{OH})_y$ (25–600 °C) upon exposure to 250, 500 and 1000 ppm CO at 25 °C (R is resistance in CO and R_0 is resistance in background gas 21% Oxygen).

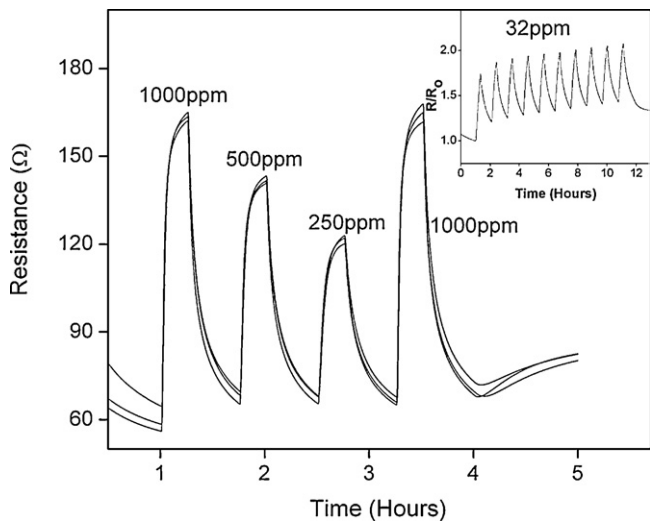


Fig. 9. Change in resistance of three different samples of $\text{RuO}_x(\text{OH})_y$ upon exposure to 1000, 500, 250 and 1000 ppm CO at 25 °C in 21% oxygen. Inset: normalized change in resistance on exposure to 32 ppm CO at 25 °C in 21% oxygen.

4.1. Reactivity of CO with $\text{RuO}_x(\text{OH})_y$

The changes in the infrared spectra in the 1000–1700 cm^{-1} region (Fig. 5b) upon exposure of $\text{RuO}_x(\text{OH})_y$ to CO suggest formation of monodentate, bidentate and bicarbonate species [31–34]. The formation of these CO_2 -derived carbonate/bicarbonate species

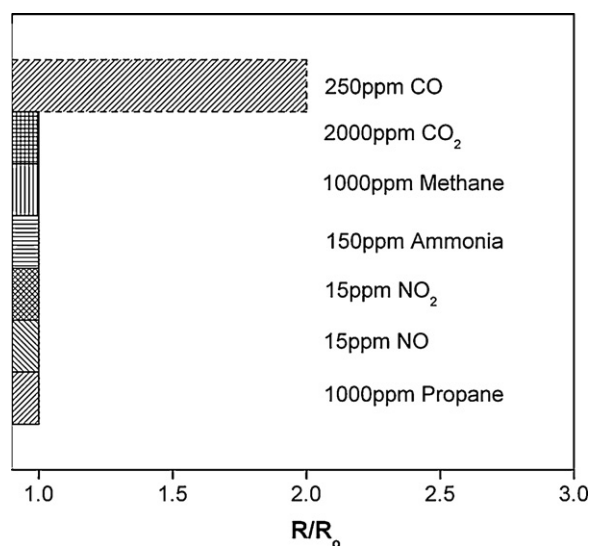
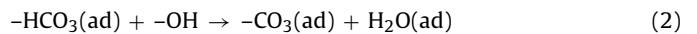
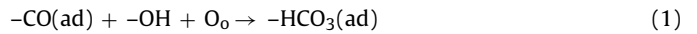


Fig. 10. Normalized change in resistance of $\text{RuO}_x(\text{OH})_y$ on exposure to 250 ppm CO, 2000 ppm CO_2 , 1000 ppm methane, 150 ppm ammonia, 15 ppm NO_2 and 15 ppm NO and 1000 ppm propane at 25 °C.

indicates that CO oxidation is taking place. Eventually with flow of air over the sample (150 min), the surface is completely regenerated (Fig. 5a). However, treatment in air for a limited time (30 min) leads to an intermediate stage in this cycle and provides more insight into the reactivity. Bands are observed due to chemisorbed CO at 2043 and 2059 cm^{-1} (Fig. 5c) which are characteristic of CO binding to a Ru site on RuO_2 [35]. In addition, the band at 2003 cm^{-1} is typical of CO adsorption on a coordinatively unsaturated Ru site on RuO_2 (oxygen vacancy) [35]. The band at 2354 cm^{-1} is due to adsorbed CO_2 since P and R branches typical of the gas phase are not being observed, and show that the regeneration of the sample in air leads to CO_2 formation. Exposure to flowing air also leads to the loss of the monodentate carbonate bands at 1433, 1311 and 1167 cm^{-1} (compare Fig. 5b and c). Interaction of the $\text{RuO}_x(\text{OH})_y$ surface with CO also leads to changes in the OH stretching region, loss of high frequency OH groups (3618 cm^{-1}) and generation of water (3367 cm^{-1}) (Fig. 5b). The surface of $\text{RuO}_x(\text{OH})_y$ is also reactive to CO_2 (Fig. 5d), and the carbonate/bicarbonate bands are similar to the partially air-treated sample after reaction with CO (Fig. 5c).

We propose the following reactions on $\text{RuO}_x(\text{OH})_y$:



The reaction with O_0 (lattice oxygen) on the $\text{RuO}_x(\text{OH})_y$ leads to reduction in the metal. It has been noted that redox active metal oxides are more active in CO oxidation since they can provide "active" oxygen and can accommodate oxygen vacancies [36,37]. Oxygen from the gas phase can replenish the oxygen vacancies and regenerate the sample. Evidence for the reduction also comes from the CO chemisorbed band at 2003 cm^{-1} (Fig. 5c), which is in the frequency range assigned to CO adsorbed on oxygen vacancies [35]. Overall, CO oxidation is leading to a reduction of the $\text{RuO}_x(\text{OH})_y$ surface, formation of CO_2 leading to carbonate/bicarbonate formation involving the OH groups of $\text{RuO}_x(\text{OH})_y$ and the oxygen vacancies are being occupied by CO. The adsorbed water is formed by reaction of bicarbonate with $-\text{OH}$.

CO oxidation over RuO_2 (110) has been studied extensively [10,38–41]. Two prominent active sites for reactive oxygen have been identified, a bridge site and oxygen on coordinatively unsaturated Ru atoms. The high catalytic activity is attributed to CO

adsorbed on the unsaturated site reacting with the oxygen on the unsaturated site or with the oxygen at the bridge site [40,41]. Thus, the mechanism is still controversial, centered on which oxygen is more reactive. Comparison of the mechanism of CO oxidation on $\text{RuO}_2(1\ 1\ 0)$ to CO oxidation on $\text{RuO}_x(\text{OH})_y$ is unclear, though, the kinetic data (activation energy) for CO reaction on single crystal $\text{RuO}_2(1\ 1\ 0)$ at 10^{-7} mbar pressure [39] was comparable to CO oxidation at ambient pressure on particles derived from a low temperature thermal treatment of $\text{RuO}_x(\text{OH})_y$ [15]. There are also other parallels: on single crystal $\text{RuO}_2(1\ 1\ 0)$ surface, the vibrations of chemisorbed CO at the oxygen vacancy sites are observed at 1995, 2072 and $2135\ \text{cm}^{-1}$ [35,38], we observe bands at 2003, 2043 and $2059\ \text{cm}^{-1}$. This strongly held CO on $\text{RuO}_x(\text{OH})_y$ is not removed readily with O_2 , a similar observation is made from experiments involving reaction of CO-bound $\text{RuO}_2(1\ 1\ 0)$ with O_2 [39]. The carbonate observed upon reaction of CO_2 with $\text{RuO}_2(1\ 1\ 0)$ leads to monodentate (1216 and $1410\ \text{cm}^{-1}$) [42], with $\text{RuO}_x(\text{OH})_y$ we observe bicarbonate and bidentate carbonates (Fig. 5d).

As-synthesized $\text{RuO}_x(\text{OH})_y$ is known to be a poor CO oxidation catalyst [15], and we propose that the product of the oxidation CO_2 is held as carbonates/bicarbonates which block active surface sites. Surface poisoning has also been noted for single crystal $\text{RuO}_2(1\ 1\ 0)$ due to the formation of carbonate and bicarbonate species [42,43], with the latter being proposed as the major deactivating pathway [43]. Water adsorption on Ru sites in $\text{RuO}_2(1\ 1\ 0)$ has also been proposed to act as deactivating the catalysts [44]. Carbonate poisoning is also reported on Co_3O_4 [36]. Carbonate and bicarbonate bands are also formed on exposure of Fe_2O_3 to CO [37], and the formation of the oxygenates involve the reaction of CO_2 with –OH groups. Water production during CO oxidation on $\text{Au}/\text{Fe}_2\text{O}_3$ has been noted [31].

There are least three possible scenarios to interpret the changes in resistance observed with CO. Resistance changes due to formation of carbonate species has been noted for neodymium oxide carbonate upon exposure to CO_2 and H_2O [45]. The basis for the electrical activity was the reaction between CO_2 and surface-adsorbed OH groups. However, in the present study, no resistance change was observed upon exposure of $\text{RuO}_x(\text{OH})_y$ to CO_2 , though carbonate formation was observed. Thus, even though CO_2 reacts with the OH groups in $\text{RuO}_x(\text{OH})_y$, as in the neodymium oxide carbonate, the resistance change must arise from a different pathway in $\text{RuO}_x(\text{OH})_y$.

The second scheme is based on the supercapacitor literature related to $\text{RuO}_x(\text{OH})_y$, where electronic conductivity between the particles is proposed to occur by electron hopping across small rutile-like 20–50 nm nanocrystals in a percolative fashion, with the OH/ H_2O adsorption layer between the particles forming the barrier through which the electron needs to move [11–13]. Thus, any interference to this hopping process will decrease conductivity. As shown in Fig. 5, the IR spectra indicates that carbonates are adsorbed to the $\text{RuO}_x(\text{OH})_y$ surface in the presence of CO. The carbonates formed on the surface of $\text{RuO}_x(\text{OH})_y$ will impede the electron hopping between the RuO_2 crystallites in the $\text{RuO}_x(\text{OH})_y$ network. However, this mechanism cannot be correct, since CO_2 also creates carbonates, but results in no change in resistance.

The third scheme involves the influence of the lower valent states of ruthenium on the electronic conductivity of $\text{RuO}_x(\text{OH})_y$. In $\text{RuO}_x(\text{OH})_y$ as supercapacitor, the electron capture results in reduction of ruthenium ($\text{Ru(IV)} \rightarrow \text{Ru(III)}, \text{Ru(II)}$), indicating that multiple valences are readily accessible. The origin of electronic conduction in these mixed ion-conducting materials has been correlated with an electron hopping mechanism between the 3+ and 4+ oxidation states [46,47]. Hydrated RuO_x in hydroxyapatite has been reported to be reduced by CO under ambient conditions to a lower valence state [48], and reduction of the RuO_2 layer on ruthenium catalysts during CO oxidation has also been observed [35]. Impedance spec-

troscopic studies on $\text{RuO}_2-\text{TiO}_2$ aerogels under both dry and humid conditions suggest that increase in oxygen pressure can result in electronic conductivity [49]. This increase in electronic conductivity in the presence of O_2 has been explained as due to oxidation of Ru(III) to Ru(IV). Data presented in the present study shows that lower valent states of Ru are present in $\text{RuO}_x(\text{OH})_y$ (XPS), and the IR studies show that CO oxidation is taking place, abstracting oxygen from $\text{RuO}_x(\text{OH})_y$ and leading to reduction of the material. The lower valent states of Ru will lead to increased resistance which is reverted in the presence of oxygen, as the vacancies are filled and the adsorbed carbonates/bicarbonates/water is lost.

With heated samples of $\text{RuO}_x(\text{OH})_y$, the conductivity changes observed under ambient conditions in the presence of CO gradually disappears. There are four changes that occur upon heating $\text{RuO}_x(\text{OH})_y$ —loss of water and the hydroxyl groups (as evidenced by TGA), the lower valent states of ruthenium are transformed to Ru(IV) (XPS) and the disordered RuO_x units assemble to form crystalline RuO_2 (XRD) and there is an increase of particle size with annealing (XRD). With heating of $\text{RuO}_x(\text{OH})_y$, it is reported that the CO oxidation at ambient conditions is diminished, and the reason proposed is that the surface area of the material is decreasing [15]. It is known that bulk crystalline RuO_2 is a metal and thus electron compensation upon CO oxidation can readily occur. We propose that this is the primary reason why there is only a minimal change in conductivity with CO (Fig. 8).

4.2. Sensor performance

The response of the device to CO (32–1000 ppm) as observed in Figs. 3 and 9 shows stability with repeated cycling, though passing dry gases over the sample for times >16 h does begin to decrease the signal. This loss in signal with long testing times could be due to loss of hydroxyl groups, or due to strong adsorption of carbonate species that are not being removed by the air treatment, as evidenced in the infrared (Fig. 5). An experiment was carried out where a sample was exposed to dry air for 16 h and then the sensing tests were performed. The sensor performed as well as a sensor that was not subjected to flowing gas. Thus, we propose that the sensor may be losing response at long times because of the carbonate adsorption, and inclusion of catalysts on the ruthenium oxide surface may alleviate this problem. The reproducibility of device fabrication is confirmed by the testing of multiple devices (Fig. 9). The as-synthesized $\text{RuO}_x(\text{OH})_y$ without heat treatment is the most sensitive to CO and discriminates against NH_3 , NO , NO_2 , propane, methane, CO_2 which makes it attractive for use in CO detection in ambient conditions. The advantage of the present device is that it operates at room temperature requiring no heat and hence suitable for low power applications. Typically, metal oxide semiconductor sensors based on TiO_2 [16], SnO_2 [20] operate at high temperatures (>250 °C) since oxygen vacancies are necessary for electronic conduction. Also, semiconductor sensors usually show interference to other gases (e.g. hydrocarbons) that react on the oxide surface.

5. Conclusion

$\text{RuO}_x(\text{OH})_y$ was synthesized by reaction of alkali with a solution of $\text{RuCl}_3 \cdot x\text{H}_2\text{O}$. The material was amorphous with hydroxyl groups, water and mixed valent ruthenium (Ru(III) and Ru(IV)). The conductivity of the material decreased upon exposure to CO and recovered after passing air over the sample. Infrared spectroscopy showed the presence of carbonate and bicarbonates on the $\text{RuO}_x(\text{OH})_y$ surface with CO. Upon heating the $\text{RuO}_x(\text{OH})_y$, the crystalline form of RuO_2 was obtained, but this material showed no change in resistance with CO. A mechanism involving the redox state change in $\text{RuO}_x(\text{OH})_y$ upon reaction with CO is proposed for

explaining the conductivity changes. The change in conductivity of $\text{RuO}_x(\text{OH})_y$ is suitable for the detection of carbon monoxide at room temperature. The sensing tests show that the selectivity and detection limits have the potential to make this device a practical CO detector for low power applications.

Acknowledgement

We acknowledge funding from NASA for this work.

References

- [1] H. Schafer, G. Schneidereit, W. Gerhardt, Zur Chemie Der Platinmetalle. RuO_2 Chemischer Transport, Eigenschaften, Thermischer Zerfall. Zeitschrift für Anorganische und Allgemeine Chemie 319 (1963) 327–336.
- [2] L. Krusin-Elbaum, Effect of oxygen on the electrical transport in ruthenium dioxide, Thin Solid Films 169 (1989) 17.
- [3] J.M. Fletcher, W.E. Gardner, B.F. Greenfield, M.J. Holdoway, M.H. Rand, Magnetic and other studies of ruthenium dioxide and its hydrate, J. Chem. Soc. A: Inorg. Phys. Theor. (1968) 653.
- [4] S.-H. Kim, J.G. Hong, S.K. Streiffer, A.I. Kingon, The effect of RuO_2/Pt hybrid bottom electrode structure on the leakage and fatigue properties of chemical solution derived $\text{Pb}(\text{Zr}_x\text{Ti}_{1-x})_3$ thin films, J. Mater. Res. 14 (1999) 1018.
- [5] L. Chen, D. Guay, A. Lasia, Kinetics of the hydrogen evolution reaction on $\text{RuO}[\text{Sub }2]$ and $\text{IrO}[\text{Sub }2]$ oxide electrodes in H_2SO_4 solution: an AC impedance study, J. Electrochem. Soc. 143 (1996) 3576.
- [6] J. Jirkovský, H. Hoffmannová, M. Klementová, P. Krtík, Particle size dependence of the electrocatalytic activity of nanocrystalline RuO_2 electrodes, J. Electrochem. Soc. 153 (2006) E111.
- [7] S.K. Das, P.K. Dutta, Synthesis and characterization of a ruthenium oxide–zeolite Y catalyst for photochemical oxidation of water to dioxygen, Micropor. Mesopor. Mater., 22 (1998) 475–483.
- [8] P.K. Dutta, A.S. Vaidealingam, Zeolite-supported ruthenium oxide catalysts for photochemical reduction of water to hydrogen, Micropor. Mesopor. Mater., 62 (2003) 107–120.
- [9] H. Liu, E. Iglesia, Selective oxidation of methanol and ethanol on supported ruthenium oxide clusters at low temperatures, J. Phys. Chem. B 109 (2005) 2155–2163.
- [10] M. Knapp, A.P. Seitsonen, Y.D. Kim, H. Over, Catalytic activity of the $\text{RuO}_2(100)$ surface in the oxidation of CO, J. Phys. Chem. B 108 (2004) 14392–14397.
- [11] D.A. McKeown, P.L. Hagans, L.P.L. Carette, A.E. Russell, K.E. Swider, D.R. Rolison, Structure of hydrous ruthenium oxides: implications for charge storage, J. Phys. Chem. B 103 (1999) 4825–4832.
- [12] J.P. Zheng, P.J. Cygan, T.R. Jow, Hydrous ruthenium oxide as an electrode material for electrochemical capacitors, J. Electrochem. Soc. 142 (1995) 2699.
- [13] C. Hu, W. Chen, K. Chang, How to achieve maximum utilization of hydrous ruthenium oxide for supercapacitors, J. Electrochem. Soc. 151 (2004) A281.
- [14] K. Lin, K. Chang, C. Hu, Y. Li, Mesoporous RuO_2 for the next generation supercapacitors with an ultrahigh power density, Electrochim. Acta 54 (2009) 4574–4581.
- [15] L. Zang, H. Kisch, Room temperature oxidation of carbon monoxide catalyzed by hydrous ruthenium dioxide, Angew. Chem. 39 (2000) 3921–3922.
- [16] X. Li, R. Ramasamy, P.K. Dutta, Study of the resistance behavior of anatase and rutile thick films towards carbon monoxide and oxygen at high temperatures and possibilities for sensing applications, Sens. Actuators B: Chem. 143 (2009) 308.
- [17] J. Trimboli, M. Mottern, H. Verweij, P.K. Dutta, Interaction of water with titania: implications for high-temperature gas sensing, J. Phys. Chem. B 110 (2006) 5647–5654.
- [18] H. Tai, Y. Jiang, G. Xie, J. Yu, X. Chen, Fabrication and Gas sensitivity of polyaniline–titanium dioxide nanocomposite thin film, Sens. Actuators: B. Chem. 125 (2007) 644–650.
- [19] S. Zhuiykov, Carbon monoxide detection at low temperatures by semiconductor sensor with nanostructured Au-doped CoOOH films, Sens. Actuators B: Chem. 129 (2008) 431–441.
- [20] Z. Jin, H. Zhou, Z. Jin, R. Savinell, C.C. Liu, Application of nano-crystalline porous tin oxide thin film for CO sensing, Sens. Actuators B: Chem. B52 (1998) 188.
- [21] A.V. Tadeev, G. Delabougisse, M. Labeau, Sensor properties of Pt doped SnO_2 thin films for detecting CO, Thin Solid Films 337 (1999) 163–165.
- [22] R.K. Joshi, Q. Hu, F. Alvi, N. Joshi, A. Kumar, Au decorated zinc oxide nanowires for CO sensing, J. Phys. Chem. C 113 (2009) 16199–16202.
- [23] A. Salomonsson, R.M. Petoral, K. Uvdal, C. Aulin, P. Käll, L. Ojamäe, M. Strand, M. Sanati, A.L. Spetz, Nanocrystalline ruthenium oxide and ruthenium in sensing applications—an experimental and theoretical study, J. Nanopart. Res. 8 (2006) 899–910.
- [24] J.P. Zheng, T.R. Jow, A new charge storage mechanism for electrochemical capacitors, J. Electrochem. Soc. 142 (1995) L6.
- [25] D.R. Rolison, P.L. Hagans, K.E. Swider, J.W. Long, Role of hydrous ruthenium oxide in Pt–Ru direct methanol fuel cell anode electrocatalysts: the importance of mixed electron/proton conductivity, Langmuir 15 (1999) 774–779.
- [26] A. Foelske, O. Barbieri, M. Hahn, R. Kötz, An X-ray photoelectron spectroscopy study of hydrous ruthenium oxide powders with various water contents for supercapacitors, Electrochim. Solid State Lett. 9 (2006) A268.
- [27] Z.F. Yin, Y.R. Feng, W.Z. Zhao, Z.Q. Bai, G.F. Lin, Effect of temperature on CO_2 corrosion of carbon steel, Surf. Interface Anal. 41 (2009) 517–523.
- [28] D. Susanti, D.-. Tsai, Y.-. Huang, A. Korotcov, W. Chung, Structures and electrochemical capacitive properties of RuO_2 vertical nanorods encased in hydrous RuO_2 , J. Phys. Chem. C 111 (2007) 9530–9537.
- [29] S. Pylypenko, B.B. Blizanac, T.S. Olson, D. Konopka, P. Atanassov, Composition- and morphology-dependent corrosion stability of ruthenium oxide materials, ACS Appl. Interfaces 1 (2009) 604–611.
- [30] Y.J. Kim, Core-level X-ray photoelectron spectra and X-ray photoelectron diffraction of $\text{RuO}_2(110)$ grown by molecular beam epitaxy on $\text{TiO}_2(110)$, Appl. Surf. Sci. 120 (1997) 250.
- [31] S.T. Daniells, A.R. Overweg, M. Makkee, J.A. Moulijn, The mechanism of low-temperature CO oxidation with $\text{Au}/\text{Fe}_2\text{O}_3$ catalysts: a combined Mössbauer, FT-IR, and TAP reactor study, J. Catal. 230 (2005) 52–65.
- [32] C. Tseng, T.C.K. Yang, H. Wu, H. Chiang, Catalysis of oxidation of carbon monoxide on supported gold nanoparticle, J. Hazard. Mater. 166 (2009) 686–694.
- [33] A. Bensalem, B.M. Weckhuysen, R.A. Schoonheydt, Nature of adsorbed species during the reduction of $\text{CrO}_3/\text{SiO}_2$ with CO in situ FTIR spectroscopic study, J. Chem. Soc. Faraday Trans. 93 (1997) 4065–4069.
- [34] V. Galvita, L. Rihko-Struckmann, K. Sundmacher, The CO Adsorption on a $\text{Fe}_2\text{O}_3-\text{Ce}_{0.5}\text{Zr}_{0.5}\text{O}_2$ catalyst studied by TPD, isotope exchange and FTIR spectroscopy, J. Mol. Catal. A, Chem. 283 (2008) 43–51.
- [35] J. Assmann, V. Narkhede, L. Khodeir, E. Löffler, O. Hinrichsen, A. Birkner, H. Over, M. Mühl, On the nature of the active state of supported ruthenium catalysts used for the oxidation of carbon monoxide: steady-state and transient kinetics combined with in situ infrared spectroscopy, J. Phys. Chem. B 108 (2004) 14634–14642.
- [36] M.J. Pollard, B.A. Weinstock, T.E. Bitterwolf, P.R. Griffiths, A. Piers Newberry, J.B. Paine, A mechanistic study of the low-temperature conversion of carbon monoxide to carbon dioxide over a cobalt oxide catalyst, J. Catal. 254 (2008) 218–225.
- [37] N.M. Gupta, A.K. Tripathi, The role of nanosized gold particles in adsorption and oxidation of carbon monoxide over $\text{Au}/\text{Fe}_2\text{O}_3$ catalyst, Gold Bull. (London, United Kingdom) 34 (2001) 120.
- [38] J. Altmann, E. Löffler, A. Birkner, M. Mühl, Ruthenium as oxidation catalyst: bridging the pressure and material gaps between ideal and real systems in heterogeneous catalysis by applying DRIFT spectroscopy and the TAP reactor, Catal. Today 85 (2003) 235–249.
- [39] J. Wang, C.Y. Fan, K. Jacobi, G. Ertl, The kinetics of CO oxidation on $\text{RuO}_2(110)$: bridging the pressure gap, J. Phys. Chem. B 106 (2002) 3422–3427.
- [40] S. Wendt, M. Knapp, H. Over, The role of weakly bound on-top oxygen in the catalytic CO oxidation reaction over $\text{RuO}_2(110)$, J. Am. Chem. Soc. 126 (2004) 1537–1541.
- [41] M. Rieger, J. Rogal, K. Reuter, Effect of surface nanostructure on temperature programmed reaction spectroscopy: first-principles kinetic Monte Carlo simulations of CO oxidation at $\text{RuO}_2(110)$, Phys. Rev. Lett. 100 (2008) 016105.
- [42] A. Lafosse, Y. Wang, K. Jacobi, Carbonate formation on the O-enriched $\text{RuO}_2(110)$ surface, J. Chem. Phys. 117 (2002) 2823.
- [43] H. Wang, W.F. Schneider, Molecular origins of surface poisoning during CO oxidation over $\text{RuO}_2(110)$, Surf. Sci., 603 (2009) L91–L94.
- [44] U.A. Paulus, Y. Wang, S.H. Kim, P. Geng, J. Wintterlin, K. Jacobi, G. Ertl, Inhibition of CO oxidation on $\text{RuO}_2(110)$ by adsorbed H_2O molecules, J. Chem. Phys. 121 (2004) 11301–11308.
- [45] I. Djerdj, A. Haensch, D. Koziel, S. Pokhrel, N. Barsan, U. Weimar, M. Niederberger, Neodymium dioxide carbonate as a sensing layer for chemoresistive CO_2 sensing, Chem. Mater. 21 (2009) 5375–5381.
- [46] V.D. Patake, C.D. Lokhande, Chemical synthesis of nano-porous ruthenium oxide (RuO_2) thin films for supercapacitor application, Appl. Surf. Sci. 254 (2008) 2820–2824.
- [47] K.E. Swider, Aerogels as a tool to study the electrical properties of ruthenium dioxide, J. Non Cryst. Solids 225 (1998) 348.
- [48] Z. Opre, D. Ferri, F. Krumeich, T. Mallat, A. Baiker, Insight into the nature of active redox sites in Ru-containing hydroxyapatite by DRIFT spectroscopy, J. Catal. 251 (2007) 48–58.
- [49] K.E. Swider, C.I. Merzbacher, P.L. Hagans, D.R. Rolison, Synthesis of ruthenium dioxide–titanium dioxide aerogels: redistribution of electrical properties on the nanoscale, Chem. Mater. 9 (1997) 1248–1255.

Biographies

Adedunni Adeyemo received her BS degree in chemistry from Morgan State University in 2004. She is currently working on her PhD in the area of analytical chemistry with a focus on the synthesis and development of new materials for gas sensing applications.

Gary W. Hunter is the Technical Lead for the Chemical Species Gas Sensors Team and Lead for Intelligent System Hardware in the Sensors and Electronics Branch at NASA Glenn Research Center. He has led the development of sensor technology and

applied in applications such as the Space Shuttle, NASA Helios Vehicle, International Space Station, Jet Engine Test Stands, the Ford Motor Company Assembly line, and on the Ford U Car. In the nanotechnology area, his work centers on oxide nanostructures. Dr. Hunter is past Chair of the Sensors Division of the Electrochemical Society and a member of the Controls, Diagnostics, and Instrumentation Committee for the International Gas Turbine Institute.

Prabir K. Dutta received his PhD degree in chemistry from Princeton University. After four years of industrial research at Exxon Research and Engineering Company, he joined The Ohio State University, where currently he is professor of chemistry. His research interests are in the area of microporous materials, including their synthesis, structural analysis and as hosts for chemical and photochemical reactions.